Accepted manuscript (author version)

To appear in:

Iranian Journal of Earth Sciences (Iran J. Earth. Sci.)

E-ISSN: 2228-785X Print ISSN: 2008-8779

This PDF file is not the final version of the record. This version will undergo further copyediting, typesetting, and production review before being published in its definitive form. We are sharing this version to provide early access to the article. Please be aware that errors that could impact the content may be identified during the production process, and all legal disclaimers applicable to the journal remain valid.

Received: 3 February 2025

Revised: 19 August 2025

Accepted: 25 December 2025

Accepted manuscript (au

This article has license CC BY 4.0 https://creativecommons.org/licenses/by/4.0/

Accepted manuscript (author version)

DOI: https://doi.org/10.57647/ijes.2027.93881

Original Research

Cost-Effective Mapping of MVT Pb-Zn Mineralization Using ASTER Data: A Hybrid Classification and Fuzzy Logic Approach in Semnan, Iran

Soran Qaderi[1], Abbas Maghsoudi*[1], Amin Beiranvand Pour[2], Mahyar Yousefi[3]

[1]Department of Mining Engineering, Amir Kabir University of Technology, Tehran, Iran
[2]Institute of Oceanography and Environment (INOS), University Malaysia Terengganu (UMT), Terengganu, Malaysia
[3]Faculty of Engineering, Malayer University, Malayer, Iran

* Corresponding author: a_maghsoudi@aut.ac.ir

© The Author(s), 2025

Abstract

This study presents a cost-effective and practical framework for mapping the mineralization potential of Mississippi Valley-type (MVT) Pb-Zn deposits using ASTER satellite imagery in western Semnan, Iran. The workflow integrates multiple spectral processing techniques—including Principal Component Analysis (PCA), band ratios, band math, and Spectral Angle Mapper (SAM)—followed by Minimum Distance Classification (MDC) and fuzzy logic modeling. The resulting mineral prospectivity map was evaluated using a Prediction–Area (P–A) plot, yielding a normalized density index (Nd) of 3.76, which demonstrates a strong spatial correspondence between the predicted prospective zones and known mineral occurrences. The proposed approach is suitable for early-stage exploration in arid and inaccessible regions and can be readily adapted for application in other metallogenic provinces, making it a valuable tool for regional-scale mineral exploration.

Keywords: ASTER satellite imagery; Mississippi Valley-type (MVT) Pb-Zn mineralization; remote sensing; spectral processing; supervised classification; fuzzy logic; mineral prospectivity mapping; Semnan; Central Iran Zone (CIZ).

This article has license CC BY 4.0 https://creativecommons.org/licenses/by/4.0/

Accepted manuscript (author version)

Accepted manuscript (author version)

1. Introduction

Satellite-based remote sensing has become one of the most widely used tools in early-stage mineral exploration because it enables rapid, cost-effective mapping of geological units, alteration zones, and structural trends across large regions. Minerals produced during hydrothermal alteration often show diagnostic spectral responses, allowing remote sensing data to highlight areas that may be associated with ore-forming processes (Crósta et al., 2003; Hajaj et al., 2023; Qaderi et al., 2025a, b). Through appropriate processing methods, remote sensing imagery can reveal mineral assemblages linked to alteration halos and thus contribute to generating exploration-scale mineral potential maps (Pour et al., 2018; Sheikhrahimi et al., 2019; Shirmard et al., 2020; Traore et al., 2020; Moradpour et al., 2022; Atif et al., 2022; Qaderi et al., 2025c, d).

Multiple investigations have demonstrated that sensors like ASTER, Landsat-8, Sentinel-2, and WorldView-3 can effectively identify lithological and mineralogical differences when integrated with analytical approaches such as principal component analysis (PCA), band ratio techniques, and spectral angle mapper (SAM) (Pour and Hashim, 2011; Mahdavi et al., 2015; Noori et al., 2019; Sekandari et al., 2020a; Bahrami et al., 2021; Traore et al., 2022). These sensors provide broad spectral coverage, and their bands—especially in the VNIR and SWIR regions—are sensitive to absorption features of key alteration-related minerals such as iron oxides, clay minerals, and carbonates (Esmaeilzadeh et al., 2023; Salmi et al., 2025).

Mississippi Valley-type (MVT) Pb-Zn deposits represent epigenetic, stratabound mineralization typically localized within dolomitized carbonate sequences (Ma, 2018; Liu et al., 2020; Qaderi et al., 2024). MVT deposits represent a major global Pb-Zn resource, accounting for nearly one-quarter of the world's reserves (He et al., 2022; Guan et al., 2023). Dolomitization plays a significant role in metal enrichment, and MVT deposits within dolomite successions generally show higher grades than those in limestone (Leach et al., 2010; Qaderi et al., 2024). For remote sensing applications, ASTER imagery is particularly advantageous because it includes 9 SWIR bands capable of capturing vibrational absorption features associated with Al–OH, Mg–OH, Fe–OH, and CO_3-bearing minerals (Hunt, 1977; Qaderi et al., 2025d). These spectral characteristics make ASTER a practical and cost-effective dataset for mapping alteration facies relevant to carbonate-hosted deposits.

This article has license CC BY 4.0 https://creativecommons.org/licenses/by/4.0/

Accepted manuscript (author version)

The present study investigates an area situated in the northern part of the Central Iran Zone (CIZ), within western Semnan Province, where carbonate units of the Elika Formation host several fluorite, barite, and Pb-Zn occurrences (GSI, 1999). The structural setting, presence of favorable host rocks, and widespread dolomitization suggest a strong potential for MVT-type mineralization (Qaderi et al., 2025d). This research employs a hybrid image-processing strategy that integrates PCA, spectral ratios, band-math indices, and SAM using ASTER VNIR/SWIR data. Minimum distance classification (MDC) was applied to differentiate alteration-related classes, and a fuzzy logic framework was used to synthesize the results into a mineral prospectivity map.

The primary aim of this study is to establish an efficient and low-cost workflow for identifying MVT-type Pb-Zn prospective areas in regions with limited data and semi-arid conditions. This methodology is adaptable and can be applied to other metallogenic provinces hosted in carbonate formations.

2. Geology of the study area

Figure 1 illustrates the location and a simplified geological framework of the study area. The area is located in the western sector of Semnan Province, positioned along the northern margin of the Central Iran Zone (CIZ) and bordering the Alborz structural belt. It forms a transitional sector between the elevated Alborz Mountains to the north and the Dasht-e Kavir Desert to the south. The area is structurally defined by two principal fault systems—the Semnan Fault and the Attari Fault—which delineate distinct tectono-sedimentary domains (GSI, 1999; Geyer et al., 2014; Qaderi et al., 2024).

The northernmost part of the area comprises units related to the Alborz Zone, including the Kahar Formation, with green sandstones, shales, and tuff layers, and the overlying Shemshak Formation, composed of volcanic rocks, shales, and coal-bearing sandstones. Southward, within the main CIZ domain, Mesozoic to Cenozoic marine and continental sedimentary sequences are widespread. Carbonate units belonging to the Elika and Qom formations play a key role in local mineralization, hosting numerous fluorite, Pb-Zn, and barite showings.

The Elika Formation, consisting primarily of thick-bedded dolomitic limestone, is of particular economic interest. Several occurrences of fluorite and galena have been documented within this unit in areas such as Versk and Shahmirzad. The dolomitized nature of these carbonate strata,

Accepted manuscript (author version)

This article has license CC BY 4.0 https://creativecommons.org/licenses/by/4.0/

together with observed alteration patterns, makes the region an excellent candidate for evaluating remote sensing-based approaches to MVT Pb-Zn prospectivity (Bazargani-Guilani et al., 2011; Qaderi et al., 2024).

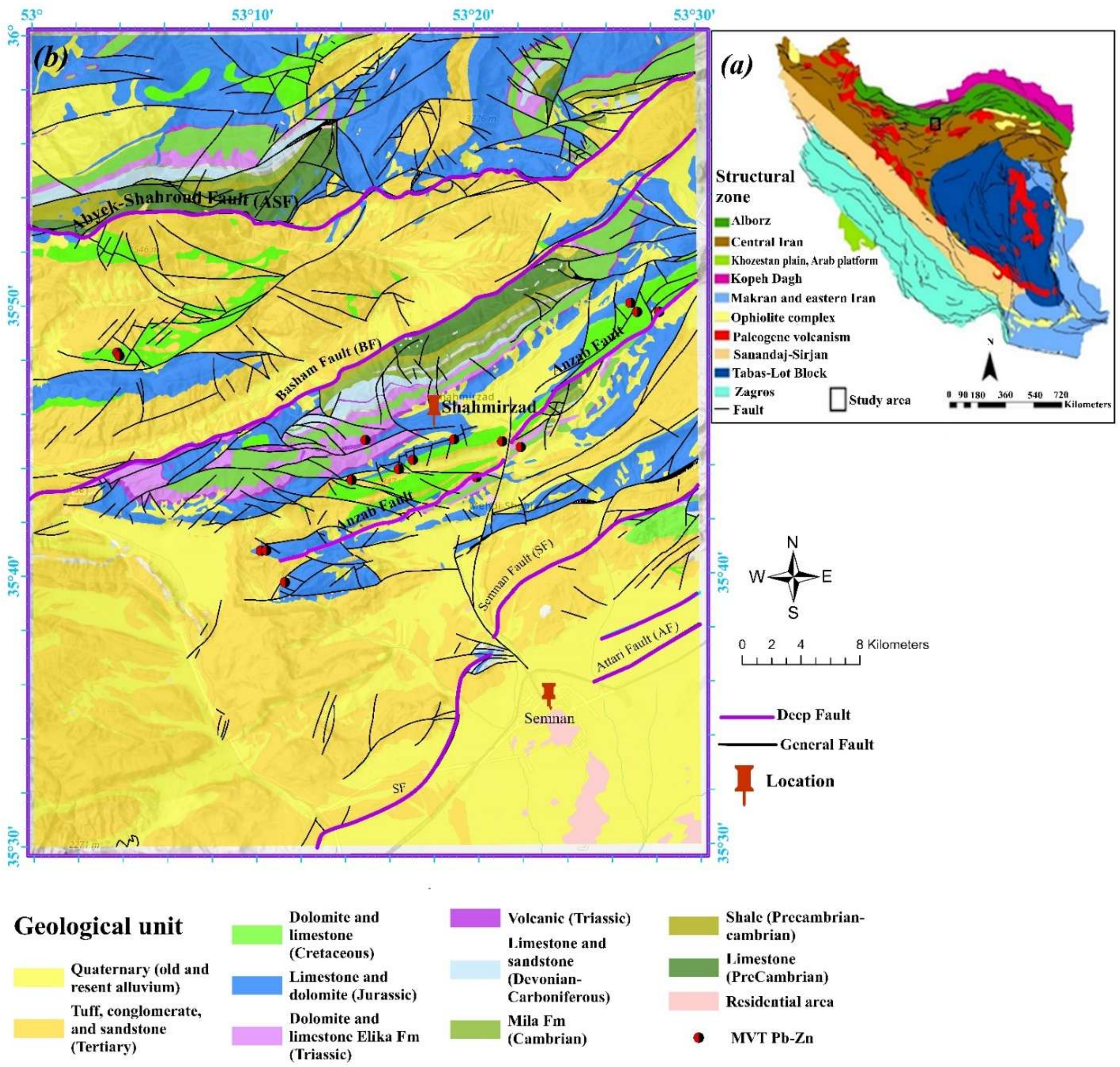

Figure 1. (a) Structural map of Iran and geographical location of the study area. (b) Simplified geological map of the study area.

This article has license CC BY 4.0 https://creativecommons.org/licenses/by/4.0/

Accepted manuscript (author version)

3. Materials and methods

3.1. Remote Sensing Data characteristics and preprocessing

ASTER, onboard NASA's Terra satellite, captures multispectral data across VNIR, SWIR, and TIR ranges using 14 distinct bands (Table 1). For this research, three cloud-free Level 1T scenes dated 20 June 2005 were obtained from the USGS Earth Explorer. Preprocessing involved band stacking, mosaicking, geometric alignment, and radiometric calibration. Atmospheric distortions were reduced through the Internal Average Relative Reflectance (IARR) method, which standardizes spectral signatures without requiring field-based calibration (Kruse et al., 1983). To harmonize spatial resolution across datasets, the SWIR bands (30 m) were resampled to the 15 m VNIR grid using the nearest-neighbor technique (Crowley, 1991).

3.2. Overall workflow

The overall methodological sequence used in this study is summarized in Fig. 2. Several spectral enhancement procedures—PCA, band ratios, band math, and SAM—were first applied to highlight alteration-related features. These enhanced layers were subsequently classified using the MDC algorithm. The classified outputs were transformed into vector layers and combined through a fuzzy logic integration scheme to produce the final mineral potential model. Known Pb–Zn occurrences were used to validate the results. Spectral operations and classification were implemented in ENVI software, whereas fuzzy logic overlay analyses were conducted in ArcMap 10.8.

Table 1. The technical characteristics of the ASTER sensor

Band	***Label***	***Wavelength (µm)***	***Resolution (m)***	***Nadir or Backward***	***Description***
B1	VNIR_Band1	0.52 - 0.60	15	Nadir	Visible green/yellow
B2	VNIR_Band2	0.63-0.69	15	Nadir	Visible red
B3N***	VNIR_Band3N	0.76–0.86	15	Nadir	Near infrared
B3B***	VNIR_Band3B	0.76–0.86	15	Backward	
B4	SWIR_Band4	1.60–1.70	30	Nadir	
B5	SWIR_Band5	2.14–2.18	30	Nadir	

This article has license CC BY 4.0 https://creativecommons.org/licenses/by/4.0/

Accepted manuscript (author version)

B6	SWIR_Band6	2.18–2.22	30	Nadir	Short-wave infrared
B7	SWIR_Band7	2.23–2.28	30	Nadir	
B8	SWIR_Band8	2.29–2.36	30	Nadir	
B9	SWIR_Band9	2.36–2.43	30	Nadir	
B10	TIR_Band10	8.12–8.47	90	Nadir	
B11	TIR_Band11	8.47–8.82	90	Nadir	
B12	TIR_Band12	8.92–9.27	90	Nadir	Long-wave infrared or thermal IR
B13	TIR_Band13	10.25–10.95	90	Nadir	
B14	TIR_Band14	10.95–11.65	90	Nadir	

* Band number 3N refers to the nadir pointing view, whereas 3B designates the backward pointing view. The visible near-infrared (VNIR), the short-wave infrared (SWIR), and the thermal-infrared (TIR) are abbreviated.

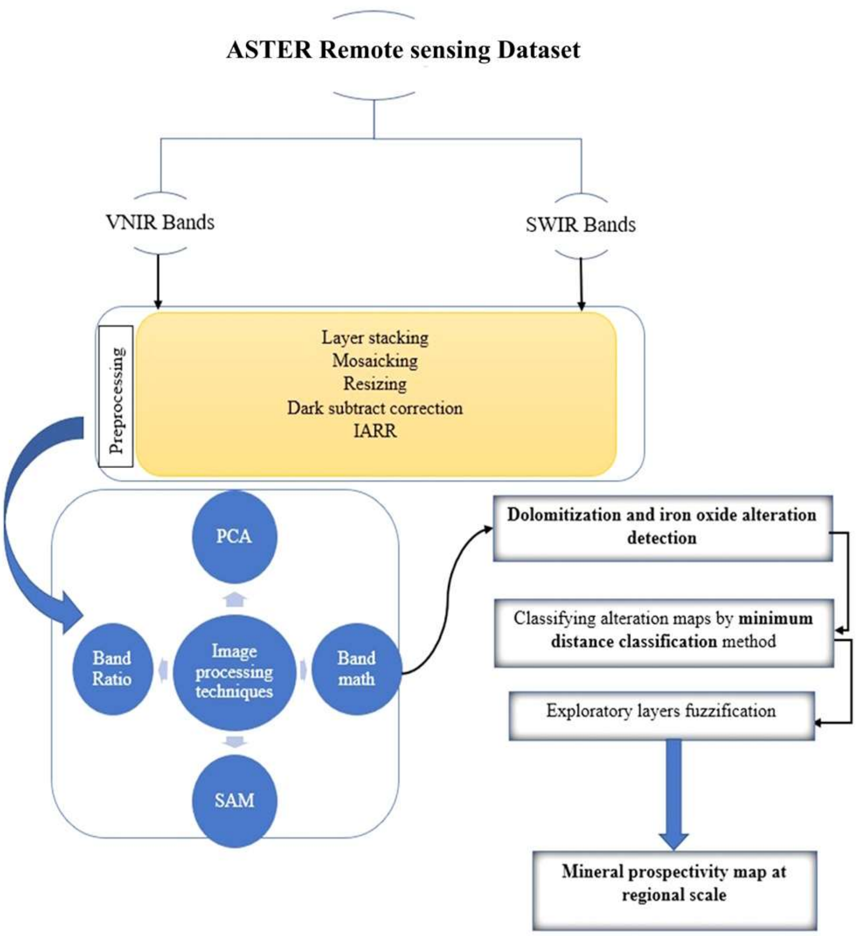

Figure 2. An overview of the methodological flowchart used in this study.

This article has license CC BY 4.0 https://creativecommons.org/licenses/by/4.0/

Accepted manuscript (author version)

3.2.1. Principal Component Analysis (PCA)

PCA reduces multiband datasets into a set of orthogonal components that maximize spectral variance (Crosta et al., 2003; Gupta et al., 2003). Depending on the objective, PCA may be performed using either the covariance or correlation matrix (Cheng et al., 2006). In mineral exploration, PCA is widely used because eigenvector loadings highlight absorption and reflectance characteristics diagnostic of alteration mineral groups (Pour and Hashim, 2014; Sheikhrahimi et al., 2019; Qaderi et al., 2025d). When a principal component exhibits large but opposite-sign loadings in relevant bands, this typically indicates that the component enhances a specific alteration mineral or mineral assemblage (Sekandari et al., 2020b). In this work, PCA was applied to the VNIR+SWIR ASTER bands. Table 2 presents the eigenvector matrix derived from these bands.

Table 2. Eigenvector matrix of ASTER VNIR + SWIR bands used in PCA for alteration detection (adopted from Qaderi et al., 2025d).

Eigenvector	***Band1***	***Band2***	***Band3***	***Band4***	***Band5***	***Band6***	***Band7***	***Band8***	***Band9***
PC1	-0.04	-0.21	-0.01	-0.99	-0.09	-0.08	-0.11	-0.14	0.01
PC2	0.35	0.01	0.23	-0.11	0.98	0.14	0.65	0.16	0.02
PC3	**-0.69**	-0.22	**0.74**	0.17	0.15	-0.17	**-0.86**	-0.02	0.11
PC4	-0.12	-0.11	0.02	0.32	-0.021	-0.16	0.98	0.05	-0.14
PC5	-0.33	-0.04	**0.52**	-0.14	-0.17	**0.63**	**-0.79**	0.53	0.16
PC6	0.52	-0.37	-0.13	0.27	0.02	-0.18	**-0.67**	**0.84**	-0.42
PC7	0.77	0.02	-0.31	0.02	-0.01	-0.01	0.11	0.25	0.57
PC8	-0.72	0.12	-0.99	0.01	0.01	0.32	-0.14	0.33	-0.02
PC9	-0.01	-0.02	-0.19	-0.29	0.01	-0.21	-0.001	0.08	0.05

3.2.2 Band Ratio

Band ratios enhance spectral differences by dividing reflectance values of one band by another. A numerator band is chosen where the target shows higher reflectivity, while the denominator corresponds to a band where absorption is stronger (Rasouli and Tangestani, 2020; Qaderi et al.,

This article has license CC BY 4.0 https://creativecommons.org/licenses/by/4.0/

Accepted manuscript (author version)

2025d). This straightforward transformation has been extensively used for lithological discrimination and alteration mapping. In this study, ratios sensitive to iron oxides, carbonates, and dolomite were selected based on their diagnostic spectral behavior (Table 3).

Table 3. Selected ASTER band ratios used for detecting alteration minerals (adopted from Qaderi et al., 2025d).

Band ratio	*Target*	*Displays color in RGB combination*
8/7	Dolomitization zones	Blue
2/1	Iron- oxides	Red
9/8	Carbonate- hosted Pb- Zn mineralization	Green

3.2.3 Band Math

Band math enables customized spectral transformations by combining multiple bands using algebraic expressions. This method is effective for enhancing subtle mineralogical contrasts, especially in arid regions where alteration minerals are well exposed (Sheikhrahimi et al., 2019; Qaderi et al., 2025d). Carbonate-rich pixels were highlighted using the expression (b7 + b9) / b8, which accentuates carbonate absorption near 2.30 µm. Dolomite was mapped using (b6 + b8) / b7 due to its distinct reflectance behavior in the 2.18–2.29 µm range. To detect ferric iron oxides and gossanous materials, the composite (b5 / b3) + (b2 / b1) was used, which captures absorption and reflectance contrasts in the visible and near-infrared wavelengths (Hunt, 1977; Qaderi et al., 2025d). Table 4 summarizes all expressions used.

Table 4. Band math expressions for mapping alteration minerals (reproduced from Qaderi et al., 2025d).

Mineral	*Band Math Relation*
Iron-Oxide	(b5/b3) + (b2/b1)
Carbonate	(b7+b9)/b8
Dolomite	(b6+b8)/b7

This article has license CC BY 4.0 https://creativecommons.org/licenses/by/4.0/

Accepted manuscript (author version)

3.2.4 Spectral Angle Mapper (SAM)

The SAM classifier computes the angular difference between each pixel spectrum and a reference endmember vector in n-dimensional spectral space (Harsanyi and Chang, 1994). Smaller angles indicate closer spectral similarity. Because SAM is based on direction rather than magnitude, it is relatively insensitive to illumination differences (Weyermann et al., 2009). In this study, dolomite mapping was performed using a USGS spectral library endmember (Fig.3).

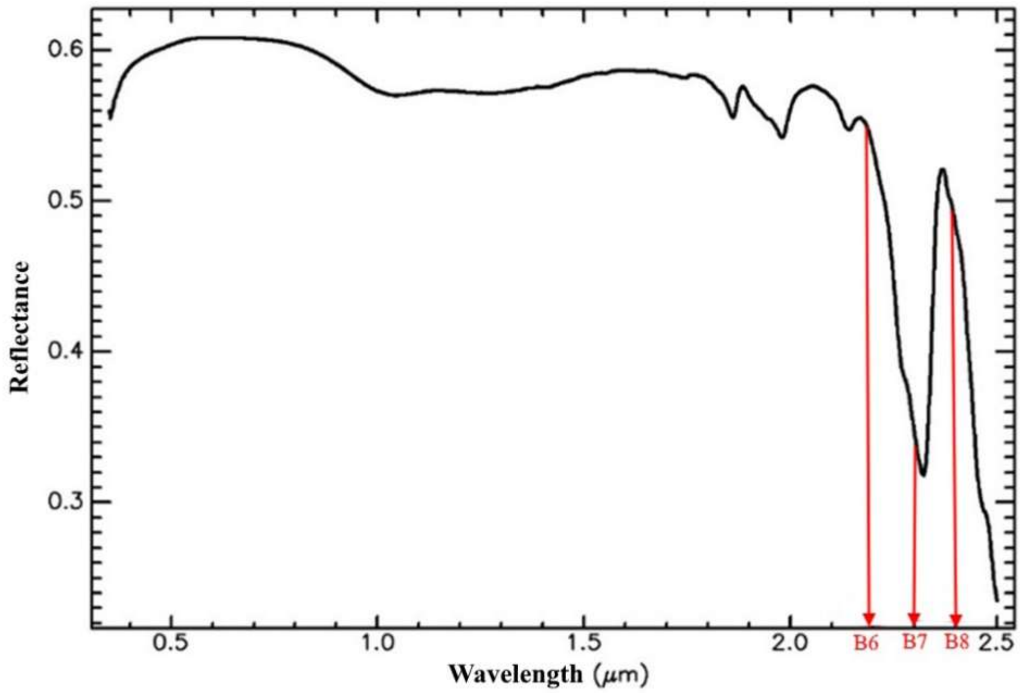

Figure 3. The reference reflectance spectra of dolomite extracted from the USGS spectral library.

3.2.5 Minimum Distance supervised Classification (MDC) Method

MDC allocates each pixel to the category whose average spectral signature lies nearest in Euclidean space. This method is computationally straightforward and proves effective when training data are scarce or when classes display moderate internal variability. Such properties make MDC particularly suitable for mineral exploration using remote sensing, as carbonate outcrops often generate strong spectral contrasts (Qaderi et al., 2025d).

This article has license CC BY 4.0 https://creativecommons.org/licenses/by/4.0/

Accepted manuscript (author version)

3.2.6 Fuzzy Logic Modeling

Fuzzy logic modeling represents a type of multi-valued logic in which variable truth values can range continuously between 0 and 1 (Novak et al., 1999). In mineral exploration, fuzzy logic combines multiple input layers through weighted evidence integration to estimate mineral potential (Yousefi and Carranza, 2015a). This approach was chosen because of its adaptability in managing uncertainty across continuous datasets and its demonstrated success in mineral prospectivity mapping. It has been effectively applied in metallogenic provinces. Typically, fuzzy logic modeling for prospectivity analysis involves three sequential steps: (i) converting evidential data into fuzzy membership values (fuzzification); (ii) integrating fuzzy maps using inference networks and suitable fuzzy set operations; and (iii) converting fuzzy outputs back into crisp values (defuzzification) to support interpretation (Sekandari et al., 2020a). Common operators for combining fuzzy membership values include fuzzy AND, fuzzy OR, fuzzy algebraic product, fuzzy algebraic sum, and fuzzy gamma (Carranza & Hale, 2001; Nykänen et al., 2008). The fuzzy gamma operator is essentially a combination of the fuzzy product and fuzzy sum, each raised to the power of gamma. The generalized function is as follows:

$$\mu(x) = (Fuzzy\ Sum)\gamma \cdot (Fuzzy\ Product)1 - \gamma \tag{1}$$

This is the specific function used by fuzzy Gamma:

$$Fuzzy\ Gamma\ Valu = pow(1 - ((1 - arg1) \cdot (1 - arg2) \cdots), \gamma) \cdot pow(arg1 \cdot arg2 \cdots, 1 - \gamma) \tag{2}$$

When gamma is set to 1, the result corresponds to the fuzzy Sum, whereas a gamma value of 0 produces the fuzzy Product. Intermediate values enable the integration of evidence between these two limits, yielding outcomes distinct from fuzzy OR or fuzzy AND. Essentially, the fuzzy Gamma operator balances the amplifying influence of the fuzzy Sum with the diminishing effect of the fuzzy Product. Figure 4 illustrates how gamma relates to both the fuzzy Sum and fuzzy Product functions.

This article has license CC BY 4.0 https://creativecommons.org/licenses/by/4.0/

Accepted manuscript (author version)

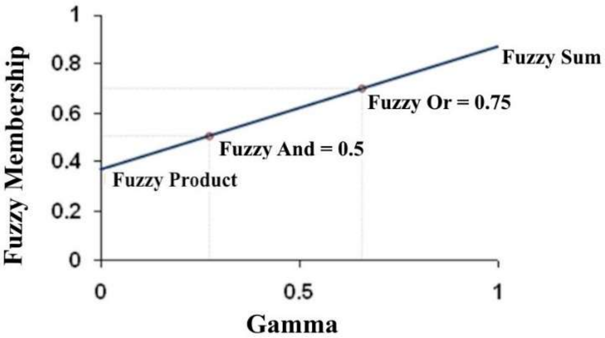

Figure 4. Relationship of fuzzy Gamma to other fuzzy membership types.

4. Results and analysis

4.1 Image processing outputs

Evaluation of PCA eigenvectors (Table 2) indicates that several components effectively isolate spectral features associated with iron oxides, dolomite, and carbonate units. Iron oxides—characterized by charge-transfer and crystal-field absorptions (Hunt and Ashley, 1979)—correspond to ASTER VNIR bands 1 and 3, while jarosite exhibits absorptions near 0.43, 0.50, 0.90 and 2.30 µm (Cloutis et al., 2006). Carbonates display diagnostic absorptions linked to vibrational modes of the CO_3 group in bands 6, 7, and 8, with dolomite showing deeper features around 2.30 µm compared with calcite (Crowley, 1991).

PC3 exhibited strong negative loadings in bands 1 and 7 and a strong positive loading in band 3, effectively enhancing iron oxide–rich pixels. PC5 emphasized dolomite-bearing units through positive loadings in bands 3 and 6 and a large negative value in band 7. PC6 enhanced general carbonate units based on the contrast between bands 7 and 8. Fig. 5 presents thematic maps generated from PC3, PC5, and PC6.

Complementary band ratios (2/1 for iron oxides, 9/8 for carbonates, and 8/7 for dolomite) and band math expressions ((5/3) + (2/1); (7+9)/8; (6+8)/7) further refined alteration detection (Fig. 6a–b). SAM classification (Fig. 6c) produced dolomite signatures consistent with PCA and ratio-based outputs, although with slight variations across the southwestern and northeastern sectors.

4.2 MDC

Accepted manuscript (author version)

This article has license CC BY 4.0 https://creativecommons.org/licenses/by/4.0/

Accepted manuscript (author version)

The MDC classifier was applied to PCA, band ratio, and band math outputs. Six thematic classes were generated: (1) iron oxide, (2) carbonate–dolomite, (3) iron oxide + carbonate, (4) iron oxide + dolomite, (5) carbonate, and (6) dolomite. Fig. 7 illustrates the classification results.

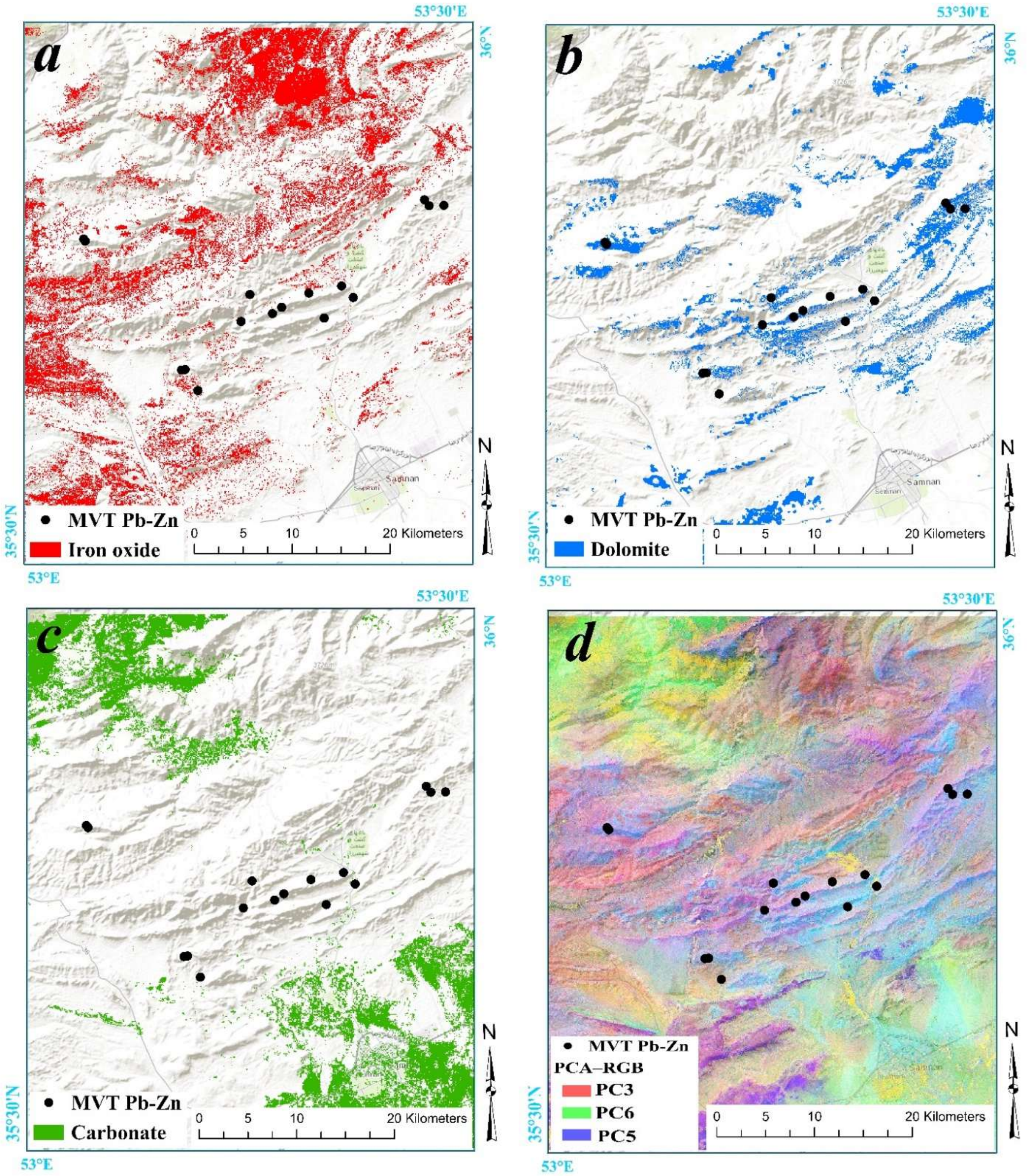

Figure 5. Image-map of (a) PC3, (b) PC5, (c) PC6, and (d) RGB image-map of PC3, PC6 and PC5. Circles show the spatial locations of Pb/Zn mineralization.

This article has license CC BY 4.0 https://creativecommons.org/licenses/by/4.0/

Accepted manuscript (author version)

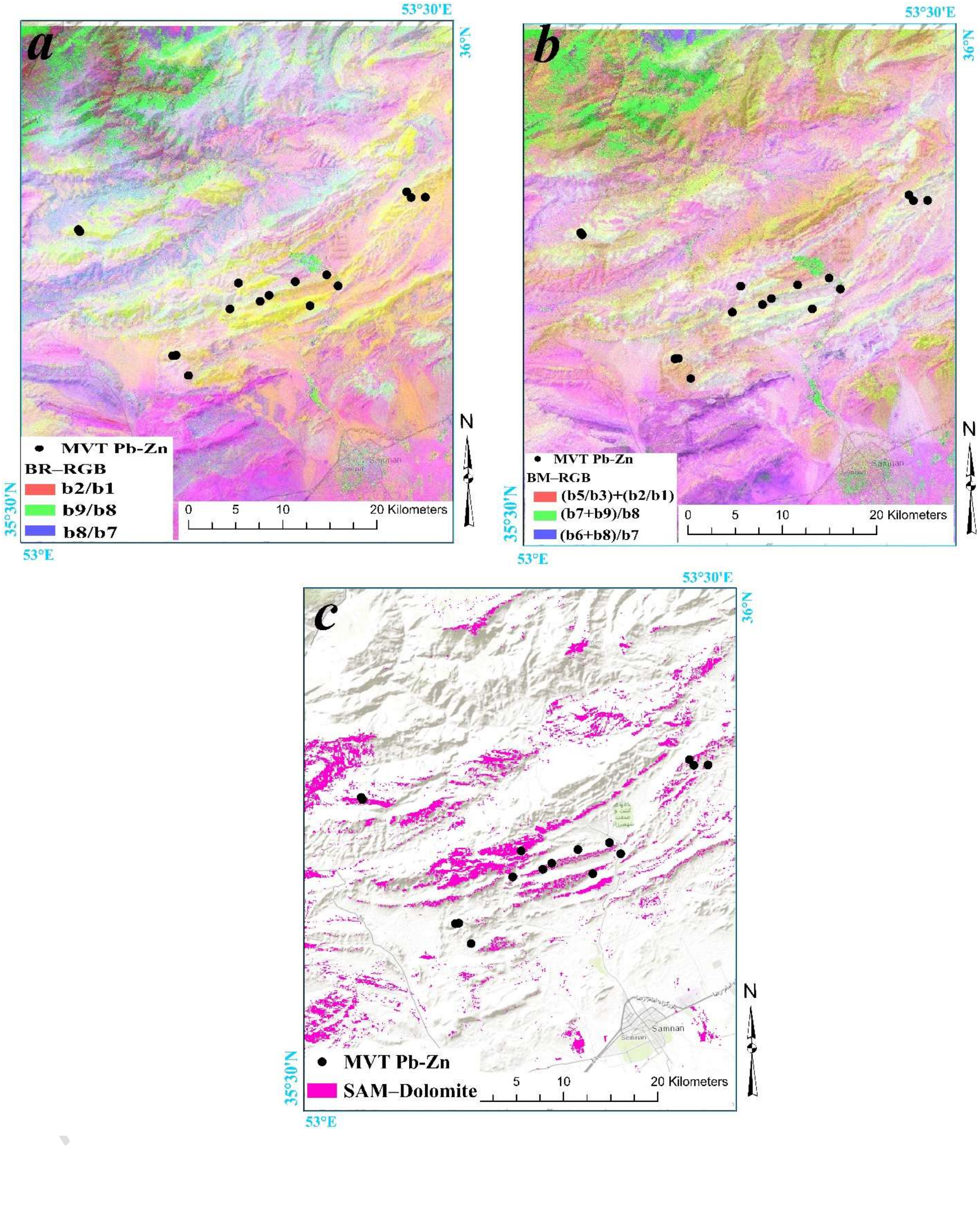

Figure 6. (a) band ratio RGB image-map of 2/1, 9/8, and 8/7, (b) band math RGB image-map of (5/3) + (2/1), (7+9)/8, and (6+8)/7, (c) SAM image-map of dolomite. Circles show the spatial locations of Pb-Zn mineralization.

This article has license CC BY 4.0 https://creativecommons.org/licenses/by/4.0/

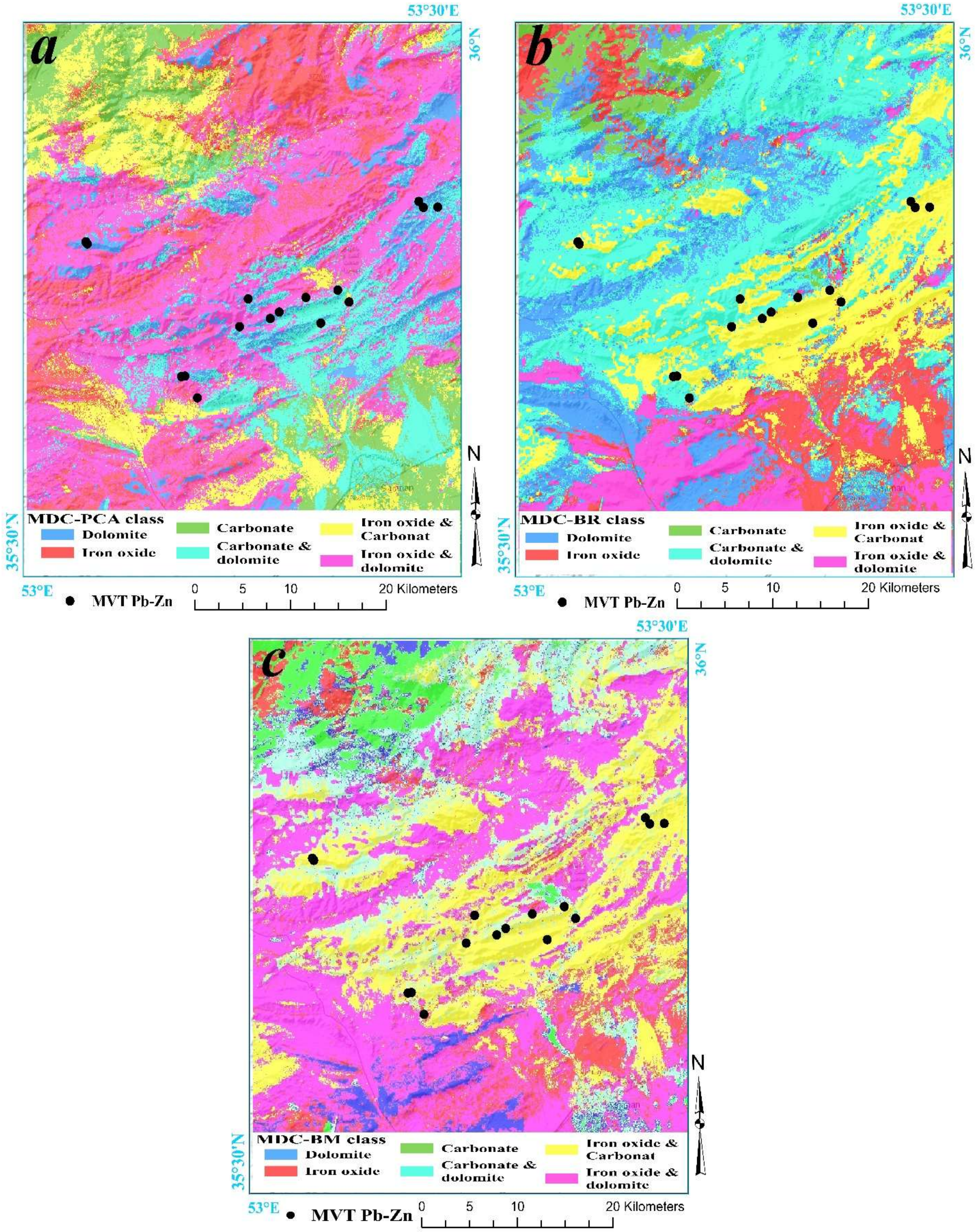

Figure 7. (a) MDC of PCA, (b) MDC of band ratio, (c) MDC of band math. Circles show the spatial locations of Pb-Zn mineralization.

This article has license CC BY 4.0 https://creativecommons.org/licenses/by/4.0/

Accepted manuscript (author version)

4.3. Mineralization modeling

Spectrally derived dolomite and iron-oxide layers—obtained from MDC-PCA, MDC-BR, MDC-BM, and SAM—were selected as the evidential inputs for predicting MVT Pb–Zn prospectivity. Each layer was standardized to a 0–1 fuzzy membership scale (Table 5), and the fuzzy gamma operator was employed to integrate them. The resulting prospectivity map (Fig. 8a) delineates zones of high to low potential for Pb-Zn mineralization. The high-potential regions display strong spatial agreement with documented mineral occurrences. Model performance was quantitatively evaluated using the Prediction–Area (P–A) plot (Yousefi and Carranza, 2015b). The P–A plot compares the cumulative proportion of known mineral occurrences captured (Pr curve) with the cumulative area predicted as prospective (Oa curve). The normalized density index (Nd)—defined at the intersection of these curves—was used to measure model efficiency. Values above 1 indicate meaningful spatial concentration of known deposits within limited high-potential areas. The computed Nd value of 3.76 demonstrates excellent alignment between predicted high-potential zones and known MVT Pb-Zn occurrences, confirming the robustness of the proposed workflow (Fig. 8b).

Table 5. Fuzzification parameters for the input layers.

Data origin	***Evidence layer***	***Mineral target***	***Classification applied***	***Membership type***
ASTER dataset	PC5	Dolomite	MDC	Small
	Band math ((b6 + b8)/b7)	Dolomite	MDC	Small
	SAM	Dolomite	Not required	Small
	Band ratio (8/7)	Dolomite	MDC	Small
	PC3	Iron-oxide	MDC	Small
	Band math (5/3) + (2/1)	Iron-oxide	MDC	Small
	Band ratio (2/1)	Iron-Oxide	MDC	Small

This article has license CC BY 4.0 https://creativecommons.org/licenses/by/4.0/

Accepted manuscript (author version)

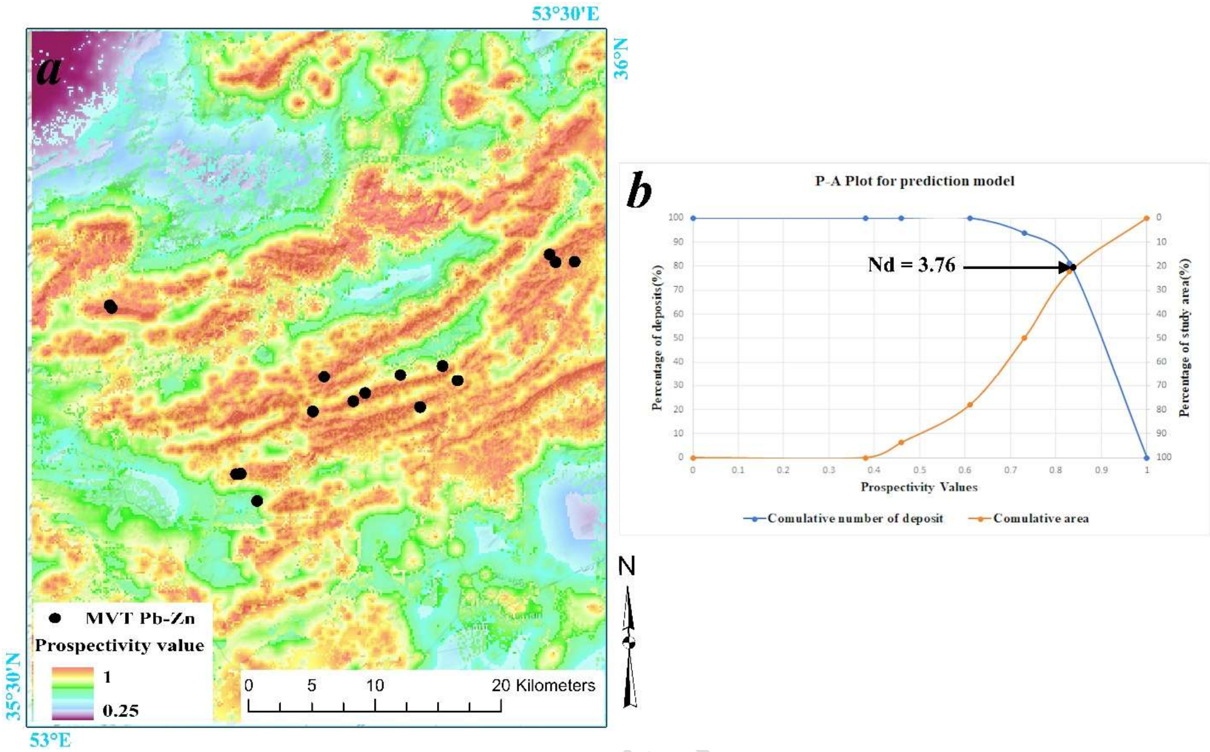

Figure 8. (a) MDC–MDC-based continuous prospectivity of the study area, (b). P–A plot for the prospectivity map.

5. Discussion

Recent advances in mineral exploration increasingly emphasize the integration of geochemical, geophysical, geological, and remote sensing datasets through sophisticated data-driven approaches (Bahrami et al., 2021; Qaderi and Maghsoudi, 2025a, b). Although such multi-source systems generally enhance prediction accuracy, they require considerable resources and may be impractical in remote or rugged regions (Carranza, 2011; Yousefi and Nykänen, 2017; Qaderi et al., 2025e). By contrast, remote sensing offers an efficient first-pass exploration method with broad coverage and low acquisition costs (Pour et al., 2014; Liu et al., 2023; Guan et al., 2023; Hegab, 2024).

The hybrid framework proposed here—combining spectral enhancement techniques, MDC, and fuzzy logic integration—proved highly effective for identifying MVT Pb-Zn targets in western Semnan. The strong Nd value (3.76) and correspondence with favorable host rocks and structural trends indicate that the model accurately delineates zones of elevated prospectivity.

This article has license CC BY 4.0 https://creativecommons.org/licenses/by/4.0/

Accepted manuscript (author version)

While the results are promising, several limitations warrant consideration. The accuracy of mapping may be affected by the quality of ASTER imagery, positional uncertainty in the mineral occurrence dataset, and the use of spectral library endmembers rather than field-measured spectra for SAM classification. Future work incorporating hyperspectral datasets or locally collected spectral signatures could enhance classification accuracy.

The resulting mineral potential map provides a valuable decision-support tool for early exploration and target prioritization. The workflow is adaptable, low-cost, and scalable, making it suitable for application in other carbonate-hosted metallogenic settings.

6. Conclusions

This study highlights the value of ASTER VNIR–SWIR data, combined with classical spectral processing techniques, for mapping Mississippi Valley-type (MVT) Pb-Zn mineralization potential in western Semnan. By integrating PCA, band ratios, band math, SAM, MDC, and fuzzy logic modeling, a high-quality mineral prospectivity map was generated.

The methodology demonstrated strong predictive capability, as evidenced by an Nd value of 3.76 on the P–A plot and close spatial agreement with documented ore occurrences. The workflow is practical, cost-effective, and transferable, offering a reliable early-stage exploration tool for carbonate-hosted lead–zinc systems.

Future studies should consider the use of hyperspectral imagery, machine learning classifiers, and field-based validation to further refine mineral detection accuracy and strengthen regional exploration models.

References

Aali, A.A., Shirazy, A., Shirazi, A., Pour, A.B., Hezarkhani, A., Maghsoudi, A., Hashim, M., & Khakmardan, S. (2022). Fusion of Remote Sensing, Magnetometric, and Geological Data to Identify Polymetallic Mineral Potential Zones in Chakchak Region, Yazd, Iran. *Remote Sensing* 14 (23), 6018. https://doi.org/10.3390/rs14236018

Abedi, M., Abedi, M., Kashani, S.B., Norouzi, G., & Yousefi, M. (2017). A deposit scale mineral prospectivity analysis: A comparison of various knowledge-driven approaches for porphyry

This article has license CC BY 4.0 https://creativecommons.org/licenses/by/4.0/

Accepted manuscript (author version)

copper targeting in Seridune, Iran. *Journal of African Earth Sciences* 128: 127-146. https://doi.org/10.1016/j.jafrearsci.2016.09.028

Atif, Y., Soulaimani, A., Lamqadem, A. A., Pour, A. B., Pradhan, B., Nouamane, E. A., Abdelali, K., Muslim, A. M., Hossain, M. S. (2022). Identifying hydrothermally altered rocks using ASTER satellite imageries in Eastern Anti-Atlas of Morocco: A case study from Imiter silver mine. *International Journal of Image and Data Fusion* 13(4): 337–361. https://doi.org/10.1080/19479832.2021.1958928

Bahrami, H., Esmaeili, P., Homayouni, S., Pour, A.B., Chokmani, K., Bahroudi, A. (2024). Machine Learning-Based Lithological Mapping from ASTER Remote-Sensing Imagery. *Minerals 14(2),* 202. https://doi.org/10.3390/min14020202

Bahrami, Y., Hassani, H., Maghsoudi, A. (2021). Investigating the capabilities of multispectral remote sensors data to map alteration zones in the Abhar area, NW Iran. *Geosystem Engineering 24*: 18 - 30. https://doi.org/10.1080/12269328.2018.1557083

Bazargani-Guilani, K., Nekouvaght Tak†, M.A., Faramarzi, M. (2011). Pb–Zn deposits in Cretaceous carbonate host rocks, northeast Shahmirzad, central Alborz, Iran. *Australian Journal of Earth Sciences, 58*: 297 - 307. https://doi.org/10.1080/08120099.2011.556664

Carranza, E. J. M. (2011). From predictive mapping of mineral prospectivity to quantitative estimation of number of undiscovered prospects. *Resource Geology* 61(1): 30–51. https://doi.org/10.1111/j.1751-3928.2010.00146.x

Carranza, E. J. M., Hale, M. (2001). Geologically constrained fuzzy mapping of gold mineralization potential, Bauio District, Philippines. *Natural Resources Research, 10*(2): 125–136. https://doi.org/10.1023/A:1011500826411

Cheng, Q., Jing, L., Panahi, A. (2006). Principal component analysis with optimum order sample correlation coefficient for image enhancement. *International Journal of Remote Sensing 27*(16): 3387–3401. https://doi.org/10.1080/01431160600606882

Cloutis, E. A., Hawthorne, F. C., Mertzman, S. A., Krenn, K., Craig, M. A., Marcino, D., Methot, M., Strong, J., Mustard, J. F., Blaney, D. L., et al. (2006). Detection and discrimination of sulfate

Accepted manuscript (author version)

This article has license CC BY 4.0 https://creativecommons.org/licenses/by/4.0/

Accepted manuscript (author version)

minerals using reflectance spectroscopy. *Icarus 184*(1): 121–157. https://doi.org/10.1016/j.icarus.2006.04.003

Crósta, A., Souza, F., Carlos, A., Azevedo, F., Brodie, C. (2003). Targeting key alteration minerals in epithermal deposits in Patagonia, Argentina, using ASTER imagery and principal component analysis. *International Journal of Remote Sensing, 24*(21): 4233–4240. https://doi.org/10.1080/0143116031000152291

Crowley, J. K. (1991). Visible and near-infrared (0.4–2.5 µm) reflectance spectra of playa evaporate minerals. *Journal of Geophysical Research, 96*(B9): 16231–16240. https://doi.org/10.1029/91JB01714

Esmaeilzadeh, N., Gani, N.D., Pour, A.B., Safari, M., Fam, H.J. (2023). Hydrothermal Alteration and Lithological Mapping Using Landsat-9 and Aster Remote Sensing Spectral Imagery in the Northeast Mojave Desert, California. *IGARSS 2023 - 2023 IEEE International Geoscience and Remote Sensing Symposium* 1972-1975. https://doi.org/10.1109/IGARSS52108.2023.10282311

Geological Survey of Iran (GSI). (1999). *Geological Survey of Iran (G.I.S. group)*. http://www.gsi.ir/

Geyer, G., Bayet-Goll, A., Wilmsen, M., Mahboubi, A., Moussavi-Harami, R. (2014). Lithostratigraphic revision of the middle Cambrian (Series 3) and upper Cambrian (Furongian) in northern and central Iran. *Newsletters on Stratigraphy 47*: 21–59. https://doi.org/10.1127/0078-0421/2014/0039

Guan, G., Li, S., Li, R. (2023). Mineralization process of MVT Zn-Pb deposit promoted by the adsorbed hydrocarbon: A case study from Mayuan Deposit on the North Margin of Sichuan Basin. *Minerals, 13*, 72. https://doi.org/10.3390/min13010072

Gupta, R. P., Tiwari, R. K., Saini, V., Srivastava, N. (2013). A simplified approach for interpreting principal component images. *Advances in Remote Sensing, 2*: 111–119. http://dx.doi.org/10.4236/ars.2013.22015

Hajaj, S., El Harti, A., Jellouli, A., Pour, A. B., Himyari, S. M., Hamzaoui, A., Bensalah, M. K., Benaouiss, N., & Hashim, M. (2023). HyMap imagery for copper and manganese prospecting in

This article has license CC BY 4.0 https://creativecommons.org/licenses/by/4.0/

the east of Ameln valley shear zone (Kerdous inlier, western Anti-Atlas, Morocco). *Journal of Spatial Science*. https://doi.org/10.1080/14498596.2023.2172085

Harsanyi, J. C., Chang, C. I. (1994). Hyperspectral image classification and dimensionality reduction: An orthogonal subspace projection approach. *IEEE Transactions on Geoscience and Remote Sensing, 32*(4): 779–785. https://doi.org/10.1109/36.298007

He, Z., Gao, J., Li, S., He, S. (2022). Mineralization of MVT Pb-Zn deposits in the process of hydrocarbon accumulation and destruction in the strong structural deformation area of Eastern Sichuan, South China. *Minerals, 12*, 1281. https://doi.org/10.3390/min12101281

Hegab, M.A. (2024). Mineral exploration and environmental impact assessment in the Jabal Hamadat Area, Central Eastern Desert, Egypt, using remote sensing and airborne radiometric data. *Scientific Reports, 14*. https://doi.org/10.1038/s41598-024-71387-2

Hunt, G. R. (1977). Spectral signatures of particulate minerals in the visible and near infrared. *Geophysics* 42: 501–513. https://doi.org/10.1190/1.1440721

Hunt, G. R., & Ashley, R. P. (1979). Spectra of altered rocks in the visible and near infrared. *Economic Geology* 74: 1613–1629. https://doi.org/10.2113/gsecongeo.74.7.1613

Kruse, F. A., Lefkoff, A. B., Boardman, J. B., Heidebrecht, K. B., Shapiro, A. T., Barloon, P. J., Goetz, A. F. H. (1993). The Spectral Image Processing System (SIPS) – Interactive visualization and analysis of imaging spectrometer data. *Remote Sensing of Environment* 44: 145–163. https://doi.org/10.1016/0034-4257(93)90013-N

Leach, D. L., Taylor, R. D., Fey, D. L., Diehl, S. F., Saltus, R. W. (2010). A deposit model for Mississippi Valley-type lead-zinc ores: Chapter A in *Mineral deposit models for resource assessment*. Scientific Investigations Report. https://doi.org/10.3133/sir20105070A

Liu, C., Qiu, C., Wang, L., Feng, J., Wu, S., Wang, Y. (2023). Application of ASTER Remote Sensing Data to Porphyry Copper Exploration in the Gondwana Region. *Minerals. 13(4),* 501. https://doi.org/10.3390/min13040501

Accepted manuscript (author version)

This article has license CC BY 4.0 https://creativecommons.org/licenses/by/4.0/

Accepted manuscript (author version)

Liu, Y., Yang, Z., Yue, L., Yu, Y., Ma, W., Tang, B. (2020). Geological characteristics and genesis of the Jiamoshan MVT Pb-Zn deposit, Sanjiang belt, Tibetan Plateau. *Acta Geologica Sinica - English Edition, 94 (4)*, 1238-1255. https://doi.org/10.1111/1755-6724.14562

Ma, R. (2018). Study on geological features and exploration methods of MVT Pb-Zn deposits. *IOP Conference Series: Earth and Environmental Science, 108*, 032010. https://doi.org/10.1038/s41598-024-71387-2

Mahdavi M., Dabiri R., Shah Hosseini E. (2015) Magmatic evolution and compositional characteristics of tertiary volcanic rocks associated with the venarch manganese mineralization, Sw Qom, Central Iran, Earth Sciences Research Journal, 19(2):141-145. DOI: https://doi.org/10.15446/esrj.v19n2.49372

Moradpour, H., Paydar, G. R., Feizizadeh, B., Blaschke, T., Pour, A. B., Khalil Kamran, K. V., Muslim, A. M., Hossain, M. S. (2022). Fusion of ASTER satellite imagery, geochemical, and geology data for gold prospecting in the Astaneh granite intrusive, West Central Iran. *International Journal of Image and Data Fusion* 13(1): 71–94. https://doi.org/10.1080/19479832.2021.1915395

Noori, L., Pour, B. A., Askari, G., Taghipour, N., Pradhan, B., Lee, C.-W., Honarmand, M. (2019). Comparison of different algorithms to map hydrothermal alteration zones using ASTER remote sensing data for polymetallic vein-type ore exploration: Toroud–Chahshirin Magmatic Belt (TCMB), North Iran. *Remote Sensing, 11*, 495. https://doi.org/10.3390/rs11050495

Novák, V., Perfilieva, I., Močkoř, J. (1999). *Mathematical principles of fuzzy logic*. Kluwer Academic. https://doi.org/10.1007/978-0-7923-8595-0

Nykänen, V., Groves, D. I., Ojala, V. J., Eilu, P., Gardoll, S. J. (2008). Reconnaissance-scale conceptual fuzzy-logic prospectivity modelling for iron oxide copper–gold deposits in the northern Fennoscandian Shield, Finland. *Australian Journal of Earth Sciences* 55: 25–38. https://doi.org/10.1080/08120090701581372

Pour, A. B., Park, T.-Y. S., Park, Y., Hong, J. K., Zoheir, B., Pradhan, B., Ayoobi, I., Hashim, M. (2018). Application of multi-sensor satellite data for exploration of Zn–Pb sulfide mineralization in the Franklinian Basin, North Greenland. *Remote Sensing, 10*, 1186. https://doi.org/10.3390/rs10081186

This article has license CC BY 4.0 https://creativecommons.org/licenses/by/4.0/

Accepted manuscript (author version)

Pour, B. A., Hashim, M. (2011). Identification of hydrothermal alteration minerals for exploring porphyry copper deposits using ASTER data, SE Iran. *Journal of Asian Earth Sciences* 42: 1309–1323. https://doi.org/10.1016/j.jseaes.2011.07.017

Pour, B. A., Hashim, M., Marghany, M. (2014). Exploration of gold mineralization in a tropical region using Earth Observing-1 (EO-1) and JERS-1 SAR data: A case study from Bau gold field, Sarawak, Malaysia. *Arabian Journal of Geosciences* 7: 2393–2406. https://doi.org/10.1007/s12517-013-0969-3

Qader, S., Maghsoudi, A., Yousefi, M., Pour, A.B. (2025b). Assimilation of the chronology of mineral system components in prospectivity analysis procedure for mineral exploration targeting: Adaptation of recurrent neural networks. *Journal of Geochemical Exploration, 272,* 107706. https://doi.org/10.1016/j.gexplo.2025.107706

Qaderi, S., Maghsoudi, A. (2025a). A New Supervised Learning Framework for Mineral Prospectivity Mapping: The Three-Class Labeling (3CL) Approach. *Journal of Geochemical* Exploration*, 278,* 107831. https://doi.org/10.1016/j.gexplo.2025.107831

Qaderi, S., Maghsoudi, A. (2025b). Comparative Analysis of One-Dimensional Convolutional Neural Network and Predictive Raster Averaging for MVT Pb-Zn Mineralization Using the Weighted Class Distribution Evaluation Framework. *Applied Geochemistry, 194*, 106595. https://doi.org/10.1016/j.apgeochem.2025.106595

Qaderi, S., Maghsoudi, A., Pour, A. B., Rajabi, A., Yousefi, M. (2025a). DCGAN-based feature augmentation: A novel approach for efficient mineralization prediction through data generation. *Minerals, 15*(1), 71. https://doi.org/10.3390/min15010071

Qaderi, S., Maghsoudi, A., Pour, A. B., Yousefi, M. (2024). Geological controlling factors on Mississippi Valley-Type Pb-Zn mineralization in Western Semnan, Iran. *Minerals, 14*(9), 957. https://doi.org/10.3390/min14090957

Qaderi, S., Maghsoudi, A., Pour, A.B., Yousefi, M. (2025d). Satellite-based remote sensing analysis for the exploration of MVT Pb-Zn mineralization using an integrated approach of Minimum Distance Classification, Deep Autoencoder and Fuzzy Logic Modeling. *Remote Sensing*

This article has license CC BY 4.0 https://creativecommons.org/licenses/by/4.0/

Applications: Society and Environment, *38(23),* 101561. https://doi.org/10.1016/j.rsase.2025.101561

Qaderi, S., Maghsoudi, A., Pour, A.B., Yousefi, M. (2025e). Advancing mineral prospectivity mapping through data augmentation and feature expansion techniques: A tabular GAN-CNN procedure. *China Geology*. https://doi/10.31035/cg20250035

Qaderi, S., Maghsoudi, A., Yousefi, M., Pour, A.B. (2025c). Translation of mineral system components into time step-based ore-forming events and evidence maps for mineral exploration: Intelligent mineral prospectivity mapping through adaptation of recurrent neural networks and random forest algorithm. *Ore Geology Reviews, 179,* 106537. https://doi.org/10.1016/j.oregeorev.2025.106537

Rasouli Beirami, M., Tangestani, M. (2020). A new band ratio approach for discriminating calcite and dolomite by ASTER imagery in arid and semiarid regions. *Natural Resources Research, 29*, 2949–2965. https://doi.org/10.1007/s11053-020-09648-w

Salmi, S., Errami, E., Jouhari, A., Lentz, D.R., Essalhi, M., Outaaoui, O., Ennih, N., Ouhoussa, L., Karfal, A. (2025). Quantification of hydrothermal alteration in Co-Ni-rich mineralized structures along fault segments crossing the Aït Ahmane and Ousdrat plutons, Bou Azzer El-Graara inlier, Central Anti-Atlas: Implications for genesis and mineral exploration. *Journal of Geochemical Exploration*. https://doi.org/10.1016/j.gexplo.2025.107712

Sekandari, M., Masoumi, I., Muslim, A. M., Hossain, M., Misra, A. (2020a). ASTER and WorldView-3 satellite data for mapping lithology and alteration minerals associated with Pb-Zn mineralization. *Geocarto International* 37: 1–23. https://doi.org/10.1080/10106049.2020.1790676

Sekandari, M., Masoumi, I., Pour, A. B., Muslim, A. M., Rahmani, O., Hashim, M., Zoheir, B., Pradhan, B., Misra, A., Aminpour, S. M. (2020b). Application of Landsat-8, Sentinel-2, ASTER and WorldView-3 spectral imagery for exploration of carbonate-hosted Pb-Zn deposits in the Central Iranian Terrane (CIT). *Remote Sensing, 12*, 1239. https://doi.org/10.3390/rs12081239

Sheikhrahimi, A., Pour, A. B., Pradhan, B., Zoheir, B. (2019). Mapping hydrothermal alteration zones and lineaments associated with orogenic gold mineralization using ASTER data: A case

Accepted manuscript (author version)

This article has license CC BY 4.0 https://creativecommons.org/licenses/by/4.0/

Accepted manuscript (author version)

study from the Sanandaj-Sirjan Zone, Iran. *Advances in Space Research* 63: 3315–3332. https://doi.org/10.1016/j.asr.2019.01.035

Shirmard, H., Farahbakhsh, E., Pour, A. B., Muslim, A. M., Müller, R. D., Chandra, R. (2020). Integration of selective dimensionality reduction techniques for mineral exploration using ASTER satellite data. *Remote Sensing, 12*, 1261. https://doi.org/10.3390/rs12081261

Traore, M., Çan, T., Tekin, S. (2022). Mapping carbonate-hosted Pb-Zn mineralization zones in Yahyali Province (Eastern Taurus, Turkey) using ASTER data. *Advances in Space Research* 69: 266–281. https://doi.org/10.1016/j.asr.2021.07.034

Traore, M., Takodjou Wambo, J. D., Ndepete, C. P., Tekin, S., Pour, A. B., Muslim, M. A. (2020). Lithological and alteration mineral mapping for alluvial gold exploration in the southeast of the Birao area, Central African Republic, using Landsat-8 Operational Land Imager (OLI) data. *Journal of African Earth Sciences, 170*, 103933. https://doi.org/10.1016/j.jafrearsci.2020.103933

Weyermann, J., Schlapfer, D., Hueni, A., Kneubuhler, M., Schaepman, M. (2009). Spectral Angle Mapper (SAM) for anisotropy class indexing in imaging spectrometry data. In *Imaging Spectrometry XIV* (Vol. 7457, p. 74570B). International Society for Optics and Photonics. https://doi.org/10.1117/12.825991

Yousefi, M., Carranza, E. J. (2015a). Fuzzification of continuous-value spatial evidence for mineral prospectivity mapping. *Computers and Geosciences* 74: 97–109. https://doi.org/10.1016/j.cageo.2014.10.014

Yousefi, M., Carranza, E. J. (2015b). Prediction-area (P-A) plot and C-A fractal analysis to classify and evaluate evidential maps for mineral prospectivity modeling. *Computers and Geosciences* 79: 69-81. https://doi.org/10.1016/j.cageo.2015.03.007

Yousefi, M., Nykänen, V. (2016). Data-driven logistic-based weighting of geochemical and geological evidence layers in mineral prospectivity mapping. *Journal of Geochemical Exploration, 164*, 94–106. https://doi.org/10.1016/j.gexplo.2015.10.008

Yousefi, M., Nykänen, V. (2017). Introduction to the special issue: GIS-based mineral potential targeting. *Journal of African Earth Sciences* 128: 1–4. https://doi.org/10.1016/j.jafrearsci.2017.02.023

This article has license CC BY 4.0 https://creativecommons.org/licenses/by/4.0/